Title: An ultrafast symmetry switch in a Weyl semimetal

Authors: Edbert J. Sie[1,2]*, Clara M. Nyby[3]*, C. D. Pemmaraju[2], Su Ji Park[2], Xiaozhe Shen[4], Jie Yang[4,5], Matthias C. Hoffmann[4], B. K. Ofori-Okai[4,10], Renkai Li[4], Alexander H. Reid[4], Stephen Weathersby[4], Ehren Mannebach[6], Nathan Finney[7], Daniel Rhodes[8,a], Daniel Chenet[7], Abhinandan Antony[7], Luis Balicas[8], James Hone[7], Thomas P. Devereaux[1,2], Tony F. Heinz[2,5,9], Xijie Wang[4], Aaron M. Lindenberg[2,5,6]†

Affiliations:

[1] Geballe Laboratory for Advanced Materials, Stanford University, Stanford, CA 94305, USA.
[2] SIMES, SLAC National Accelerator Laboratory, Menlo Park, CA 94025, USA.
[3] Department of Chemistry, Stanford University, Stanford, CA 94305, USA.
[4] SLAC National Accelerator Laboratory, Menlo Park, CA 94025, USA.
[5] PULSE Institute, SLAC National Accelerator Laboratory, Menlo Park, CA 94025, USA.
[6] Department of Materials Science and Engineering, Stanford University, Stanford, CA 94305, USA.
[7] Department of Mechanical Engineering, Columbia University, New York, NY 10027, USA.
[8] National High Magnetic Field Laboratory and Department of Physics, Florida State University, Tallahassee, FL 32310, USA.
[9] Department of Applied Physics, Stanford University, Stanford, CA 94305, USA.
[10] Department of Chemistry, Massachusetts Institute of Technology, Cambridge, MA 02139, USA.
[a] Present address: Department of Mechanical Engineering, Columbia University, New York, NY 10027, USA.

* These authors contributed equally to this work
† Correspondence to: aaronl@stanford.edu

Abstract:

Topological quantum materials possess some of the most fascinating properties of matter [1-3], with important applications for dissipationless electronics and fault-tolerant quantum computers [4, 5]. Manipulating the topological invariants in these materials is of great interest because it would allow for topological switching applications analogous to switching of transistors [6]. Lattice strain provides the most natural means of tuning these topological invariants, as it directly modifies the electron-ion interactions and potentially alters the underlying crystalline symmetry on which the topological properties depend [7-9]. However, conventional means of applying strain through heteroepitaxial lattice mismatch [10] and dislocations [11] are not extendable to controllable time-varying protocols. In particular, integration into a functional device requires the ability to go beyond the robust, topologically protected properties and discover ways to manipulate the topology at high speeds. Here, we demonstrate that terahertz (THz) light pulses can be used to induce THz frequency interlayer shear strain on a Weyl semimetal WTe_2 with large strain amplitudes, as crystallographically measured using relativistic electron diffraction, leading to a topologically distinct metastable phase. Separate nonlinear

optical measurements indicate that this transition is associated with a symmetry change to a centrosymmetric, topologically trivial phase. We further show that such shear strain serves as an ultrafast, energy-efficient means to induce more robust, well-separated Weyl points or to annihilate all Weyl points of opposite chirality. This work defines new possibilities for ultrafast manipulation of the topological properties in solids and for a topological switch operating at THz frequencies.

Main Text:

Topological materials provide a novel platform to pursue exotic physics from the seemingly distant field of particle physics in condensed matter systems, such as Weyl fermions [12-14]. This has led to a worldwide effort focused on discovering new topological quantum materials. One prime example is WTe_2, which is a layered transition-metal dichalcogenide (TMD) that crystalizes in a distorted hexagonal net with an orthorhombic unit cell (Fig. 1a) [15]. The lack of inversion symmetry in this material leads to a topological semimetal that was predicted [16] and experimentally verified [17-19] with type-II Weyl points (WPs), which can be manipulated through atomic-scale lattice distortions. In our experiments, the measured shear displacement amplitudes (~1%) are more than sufficient to undergo a complete annihilation of the WPs or a more than two-fold increased WP separation, depending on the direction of the shear displacement. Ordinary crystals start to fracture at these strains, and conventional means of using piezoelectric transducers to induce lattice distortions typically reach ~0.05% strain [20]. The observed large strain in our experiment (~1%) is possible because we use light to generate interlayer shear strain in a weakly van der Waals-bonded 2D TMD – a method that is less susceptible to lattice damage but can significantly alter the electronic band structure.

We used a relativistic ultrafast electron diffraction (UED) technique as a probe to reconstruct the shear motion and crystallographically quantify the corresponding atomic displacements by measuring more than 200 Bragg peaks (Fig. 1b) [21] (Methods). We used two different terahertz (THz) pump excitation schemes, involving a quasi-single cycle excitation at 3 THz and a few-cycle excitation at 23 THz, both of which enable application of an all-optical bias field while minimizing interband transitions (Methods). The arrival time of the electron beam (probe) can be adjusted with respect to the THz pulses (pump) using an optical delay stage. The measured diffraction pattern in equilibrium (Fig. 1c) is consistent with the orthorhombic phase of WTe_2 (Fig. 1a), where the W-W chain direction is along the crystallographic *a*-axis with a shorter unit cell. Under applied THz pump pulses, we find that the intensities of many Bragg peaks are modulated, indicating structural changes in the WTe_2 lattice. To investigate the lattice dynamics, we show the intensity changes $\Delta I/I_0$ of several Bragg peaks as a function of time delay Δt between the THz pump and electron probe pulses (Fig. 1d-e). The time traces show coherent oscillations with a frequency of 0.24 THz (Fig. 1f), which is consistent with a low frequency interlayer shear phonon mode predicted by density functional theory (DFT) analysis (Methods).

To determine the atomic motion, we plot the measured $\Delta I/I_0$ image at 2.5 ps (Fig. 2a). We find that the changes in peak intensity alternate along the *b*-axis, while peaks (hkl) with $k = 0$ show negligible changes. This suggests that the interlayer shear displacement is along the *b*-axis. To verify this, we derive the peak intensity modulation $\Delta I/I_0$ by introducing a top layer shear displacement Δy with respect to the bottom layer into the structure factor

$$S(\Delta y) = 2\sum_{\text{top}} f_j \cos\left(2\pi\left(hx_j + ky_j\right) + \pi k \Delta y\right) \tag{1}$$

where we have used the underlying crystalline symmetry in WTe_2 to obtain the final, simplified expression (Methods). Here, the summation runs over all atoms in the top half of the unit cell (2 W and 4 Te), f_j is the atomic scattering factor, $\left(x_j\hat{a}, y_j\hat{b}, z_j\hat{c}\right)$ is the atom position in the unit cell, $hk0$ are the usual Miller indices for [001] zone axis, and the lattice constants are a = 3.477 Å, b = 6.249 Å, c = 14.018 Å. To compare this with our experiment, we calculate the peak intensity modulation $\Delta I \propto |S(\Delta y)|^2 - |S(0)|^2$ and plot the image in Figure 2b. Here, we define a positive shear displacement ($\Delta y > 0$) as shown in the inset of Figure 2e. The simulated image shows an excellent agreement with the measured image and verifies that the peak intensity modulation arises primarily from interlayer shear displacement along the *b*-axis.

We determine the shear displacement amplitude through a global fitting of many Bragg peaks between the simulated and the measured intensities as a function of time delay (Methods). The fitting results are compared in the bar charts (Fig. 2c-d), showing that the proposed interlayer shear displacement fits the experimental data very well. At low pump field of 2.6 MV/cm (23 THz), the fitting results (Fig. 2f, red) show shear displacements that oscillate between -1.7 to +3.6 pm in the early stage and gradually develop an offset toward positive shear displacement of +1.5 pm in the later stage. Increasing the pump field to 7.5 MV/cm (Fig. 2f, blue) leads to a much larger offset of +8.0 pm (1.3% strain) that gradually builds up on a timescale of 25 ps and persists longer than 70 ps. The long-lived offset indicates that the lattice has found a new equilibrium position, deviating from the simple harmonic oscillator behavior normally expected. The shear oscillation frequency softens at increasing field strengths (Extended Fig. 7a-b), consistent with an anharmonic response as the material is driven to large amplitudes.

To investigate the driving mechanism, we measured the shear amplitude as a function of pump field strength and polarization. We found that the amplitude increases linearly with field under different off-resonant frequencies (Fig. 3a) and is polarization isotropic (Fig. 3b-c). Moreover, the shear motion always starts towards positive displacement regardless of polarization (Fig. 3b). This behavior cannot be explained through infrared active (IR) and Raman (ISRS) mechanisms normally considered. We propose a THz field-driven charge current mechanism, as indicated by the linear response in field strength, and motivated by recent calculations that predict a Td-1T′ transition in WTe_2 via hole doping at density ~10^{20} cm^{-3} [22]. Microscopically, the applied field accelerates the electron population away from the topmost valence band, which constitutes an

interlayer antibonding orbital. This destabilizes the interlayer coupling strength and launches a shear motion along the in-plane transition pathway from an orthorhombic (Td) phase to a monoclinic and centrosymmetric (1T′) phase with a new equilibrium position ($\Delta y > 0$) (Fig. 2e and Extended Fig. 1). In our experiment, the effective hole doping density can be estimated using the Drude model, which gives a doping density of ~10^{20} cm^{-3} comparable to the impulsive driving force for the interlayer shear motion (Methods).

We note that a departure from Td phase via interlayer displacement could result in two possible phases, monoclinic 1T′ and orthorhombic 1T′(*), both of which are centrosymmetric. Unlike the 1T′ phase, the 1T′(*) phase can be reached while maintaining the orthorhombic structure (Extended Fig. 1). Although the observed long-lived offset (8 pm, Fig. 2f) is somewhat smaller than that calculated for a complete transition to the 1T′(*) phase (~10-15 pm, Fig. 2e), the measured displacement should be viewed as a lower bound due to spatial averaging of the film seen by the electron beam. This is because, under the simplistic approximation that the induced metastable phase is a centrosymmetric phase, either 1T′(*) or 1T', the volume change associated with this transformation results in a complex longitudinally heterogeneous strain profile with strain waves propagating from the interfaces [23] and complicated by substrate interactions. These processes likely underlie some of the complex longer-time-scale dynamics (~25 ps) shown in Fig 2f. This timescale is consistent with a shear wave propagation time across the sample thickness (Methods, Extended Fig. 5). This is in comparison to the recently observed photoinduced structural transition that happens rapidly in atomically-thin indium wires [24]. To further understand this, we carried out comparative measurements in a related material, $MoTe_2$, which can crystallize in the Td and 1T′ phases at different temperatures [25, 26]. Whereas in the Td phase we observe light-induced shear displacements, in the 1T′ phase we observe negligible signals (Methods). This is consistent with a mechanism in which the THz fields drive the material unidirectionally towards 1T′.

The ability to drive a shear displacement using THz pulses offers a means to manipulate the topological properties in the semimetal WTe_2 on ultrafast timescales. There are a total of eight Weyl points (WP) in the equilibrium Td phase of WTe_2 in the $k_z = 0$ plane. It is sufficient to consider two of these WPs in the $k_x, k_y > 0$ quadrant because we can obtain the remaining six WPs through time-reversal and mirror symmetries. The two WPs carry opposite chiralities associated with topological charges $\chi^- = -1$ (WP1) and $\chi^+ = +1$ (WP2) that are connected by a Fermi arc on the surface. Since the two WPs are separated mainly along k_y, we can expect large changes in the WP separation in momentum space by tuning the hopping parameters and band dispersion through interlayer shear strain along the y-axis. In this way, the induced shear strain acts on the Weyl fermions as a chiral gauge field vector potential, $\boldsymbol{A}$, because it couples to WP1 and WP2 with opposite sign in momentum space, $\boldsymbol{p} \rightarrow (\boldsymbol{p} - \chi^{\pm} e\boldsymbol{A})$.

To demonstrate this, we compute the electronic band structure in WTe_2 using first principles DFT calculations and monitor the positions of the WPs at different interlayer displacements Δy (Fig. 4a) as determined by our structural measurements. Our DFT calculations are performed using a Born-Oppenheimer approximation where electrons can instantaneously adjust to the new lattice environment. This is particularly appropriate for the interlayer shear mode because the timescale is much longer than that of the electron's, and the use of a THz pump does not create significant electronic excitation. Type-II WPs result from crossings between electron and hole bands. Hence, by mapping the energy difference between the two bands in momentum space, the positions of the WPs can be identified as the zero-energy gap position (WP1 = blue, WP2 = red). At equilibrium ($\Delta y = 0$), the WPs are separated by 0.7% of a reciprocal lattice vector $|G_2|$. At positive shear displacements, the WPs move towards each other and mutual annihilation occurs at $\Delta y = +2.2$ pm. At negative shear displacements, the WPs move away from each other, leading to a more robust topological structure with more than two-fold increased WP separation. This is consistent with the intuitive picture where positive shear moves towards a centrosymmetric and trivial phase, while negative shear moves towards a non-centrosymmetric and topological phase. At increasingly negative Δy, WP2 is approaching the mirror plane at $k_y = 0$ and eventually annihilates with its mirror image of opposite chirality. This leads to a Lifshitz transition from a topological semimetal with eight WPs to one with four WPs, achieving the minimum nonzero number of WPs allowed in a time-reversal invariant system (Fig. 4b).

While it is challenging to measure the distinct topological phases across the Lifshitz transition, we can experimentally verify the transition from a topological phase to a trivial phase using a time-resolved second harmonic generation (SHG) technique. In a situation where inversion symmetry in WTe_2 is restored, the electronic phase transition from a topological to trivial semimetal must follow. This is because the emergence of Weyl point pairs in materials is contingent on lifting the Kramers' double degeneracy of a Dirac cone by either breaking time-reversal or inversion symmetry. SHG arises from a nonzero second-order susceptibility as shown in non-centrosymmetric topological systems [27, 28]. Thus, it can be used as a sensitive probe to monitor the inversion symmetry and topological changes in WTe_2. In this measurement, we use a 2.1 μm pump pulse to induce the transition, which gives similar interlayer shear displacements induced by THz. Figure 4d shows the SHG polarization scans of WTe_2 in the absence of pump pulse (blue), which shows two lobes oriented horizontally. After the pump pulse arrives ($\Delta t = 2$ ps), the SHG vanishes almost completely in all polarizations, with magnitudes comparable to the detection noise level and to the measured SHG signal from centrosymmetric 1T′-$MoTe_2$. Figure 4e shows the measured SHG time-trace from WTe_2 at various pump field strengths. At low fields (blue and red curves), the SHG intensity oscillates with frequency of the shear mode at 0.24 THz. Of particular importance, the oscillation always starts with a reduced SHG towards a centrosymmetric structure, consistent with our UED results (Fig. 2e-f). At high field (yellow), the SHG intensity plummets drastically approaching a 100% reduction. This indicates that WTe_2

exhibits a phase transition from a non-centrosymmetric to a centrosymmetric phase, consistent with our diffraction studies, and must correspond to a topological-to-trivial phase transition.

Similar manipulations of the WPs in WTe_2 can in principle be obtained through a compressive uniaxial strain along the *a*-axis [16]. For example, at 1% uniaxial strain the WP separation is 2.2% of $|G_2|$, and annihilation of WP2 at the mirror plane occurs at 2% uniaxial strain with energy cost of 32-39 meV per unit cell. This is about 1-2 orders of magnitude larger than the energy required for a shear strain to cause the same effect (Methods), indicating that the interlayer strain provides a more energy-efficient means to manipulate the topological bandstructure. In addition, shear displacement allows manipulation of WPs at THz frequencies. This ultrafast motion of the WPs in turn is associated with a time-varying elastic gauge potential $A(t)$ and yields a pseudoelectric field $E = -\partial A/dt$, which can be used as a novel means to modulate charge density between bulk and surface [9], and for exploring effective gauge fields driven by space- and time-dependent strains [8, 9, 29, 30].

These findings offer a new promising way to enhance control over the topological properties of matter by modulating the topological invariants through field-driven lattice deformations. This leads to a significant motion of the Weyl points and an ultrafast switch to structures with topologically distinct phases, which are potentially useful for applications. In addition, it can be used to stabilize emergent topological phases at nonequilibrium in otherwise trivial materials, thus diversifying a new class of topological materials.

References:

1. M.Z. Hasan and C.L. Kane. "Colloquium: Topological insulators". *Reviews of Modern Physics* **82,** 3045-3067 (2010).
2. A.A. Burkov. "Topological semimetals". *Nat Mater* **15,** 1145-1148 (2016).
3. S. Jia, S.Y. Xu, and M.Z. Hasan. "Weyl semimetals, Fermi arcs and chiral anomalies". *Nat Mater* **15,** 1140-1144 (2016).
4. P. Roushan et al. "Topological surface states protected from backscattering by chiral spin texture". *Nature* **460,** 1106-9 (2009).
5. Z. Alpichshev et al. "STM imaging of electronic waves on the surface of Bi2Te3: topologically protected surface states and hexagonal warping effects". *Phys Rev Lett* **104,** 016401 (2010).
6. X. Qian et al. "Quantum spin Hall effect in two-dimensional transition metal dichalcogenides". *Science* **346,** 1344-7 (2014).
7. A. Cortijo et al. "Elastic Gauge Fields in Weyl Semimetals". *Phys Rev Lett* **115,** 177202 (2015).
8. A.G. Grushin et al. "Inhomogeneous Weyl and Dirac Semimetals: Transport in Axial Magnetic Fields and Fermi Arc Surface States from Pseudo-Landau Levels". *Physical Review X* **6,** 041046 (2016).
9. D.I. Pikulin, A. Chen, and M. Franz. "Chiral Anomaly from Strain-Induced Gauge Fields in Dirac and Weyl Semimetals". *Physical Review X* **6,** 041021 (2016).
10. I. Zeljkovic et al. "Strain engineering Dirac surface states in heteroepitaxial topological crystalline insulator thin films". *Nat Nanotechnol* **10,** 849-53 (2015).
11. Y. Liu et al. "Tuning Dirac states by strain in the topological insulator Bi2Se3". *Nature Physics* **10,** 294-299 (2014).
12. S.Y. Xu et al. "Discovery of a Weyl fermion semimetal and topological Fermi arcs". *Science* **349,** 613-7 (2015).

13. L.X. Yang et al. "Weyl semimetal phase in the non-centrosymmetric compound TaAs". *Nature Physics* **11,** 728-732 (2015).
14. B.Q. Lv et al. "Experimental Discovery of Weyl Semimetal TaAs". *Physical Review X* **5,** 031013 (2015).
15. M.N. Ali et al. "Large, non-saturating magnetoresistance in WTe2". *Nature* **514,** 205-8 (2014).
16. A.A. Soluyanov et al. "Type-II Weyl semimetals". *Nature* **527,** 495-8 (2015).
17. P. Li et al. "Evidence for topological type-II Weyl semimetal WTe2". *Nat Commun* **8,** 2150 (2017).
18. C.L. Lin et al. "Visualizing Type-II Weyl Points in Tungsten Ditelluride by Quasiparticle Interference". *ACS Nano* **11,** 11459-11465 (2017).
19. Y.Y. Lv et al. "Experimental Observation of Anisotropic Adler-Bell-Jackiw Anomaly in Type-II Weyl Semimetal WTe_{1.98} Crystals at the Quasiclassical Regime". *Phys Rev Lett* **118,** 096603 (2017).
20. J. Yang et al. "Elastic and electronic tuning of magnetoresistance in MoTe2". *Sci Adv* **3,** eaao4949 (2017).
21. S.P. Weathersby et al. "Mega-electron-volt ultrafast electron diffraction at SLAC National Accelerator Laboratory". *Rev Sci Instrum* **86,** 073702 (2015).
22. H.-J. Kim et al. "Origins of the structural phase transitions in MoTe2 and WTe2". *Physical Review B* **95,** 180101 (2017).
23. M. Nicoul et al. "Picosecond acoustic response of a laser-heated gold-film studied with time-resolved x-ray diffraction". *Applied Physics Letters* **98,** 191902 (2011).
24. T. Frigge et al. "Optically excited structural transition in atomic wires on surfaces at the quantum limit". *Nature* **544,** 207-211 (2017).
25. S.Y. Chen et al. "Activation of New Raman Modes by Inversion Symmetry Breaking in Type II Weyl Semimetal Candidate T'-MoTe2". *Nano Lett* **16,** 5852-60 (2016).
26. K. Zhang et al. "Raman signatures of inversion symmetry breaking and structural phase transition in type-II Weyl semimetal MoTe2". *Nat Commun* **7,** 13552 (2016).
27. T. Morimoto and N. Nagaosa. "Topological nature of nonlinear optical effects in solids". *Sci Adv* **2,** e1501524 (2016).
28. L. Wu et al. "Giant anisotropic nonlinear optical response in transition metal monopnictide Weyl semimetals". *Nature Physics* **13,** 350-355 (2016).
29. N. Levy et al. "Strain-induced pseudo-magnetic fields greater than 300 tesla in graphene nanobubbles". *Science* **329,** 544-7 (2010).
30. K.K. Gomes et al. "Designer Dirac fermions and topological phases in molecular graphene". *Nature* **483,** 306-10 (2012).

Acknowledgments:

This work is supported primarily by the U.S. Department of Energy (DOE), Office of Basic Energy Sciences, Division of Materials Sciences and Engineering, under Contract No. DE-AC02-76SF00515, SLAC National Accelerator Laboratory (SLAC), Stanford Institute for Materials and Energy Sciences (E.J.S., C.M.N., C.D.P., E.M., T.P.D., T.F.H., A.M.L.). E.J.S. acknowledges additional support from Stanford GLAM Postdoctoral Fellowship Program. C.M.N. acknowledges additional support from the NSF through a Graduate Research Fellowship (DGE-114747). T.F.H. acknowledges additional funding for analysis from the Gordon and Betty Moore Foundation EPiQS Initiative through Grant No. GBMF4545. S.J.P. is supported by the U.S. Department of Energy (DE-SC0012375). M.C.H. is supported by the U.S. Department of Energy, Office of Science, Office of Basic Energy Sciences, under Award No. 2015-SLAC-100238-Funding. N.F. acknowledges the Stewardship Science Graduate Fellowship program's support, provided under cooperative agreement number DE-NA0002135. Synthesis of $MoTe_2$ and sample preparation were supported by the U.S. Department of Energy, DE-SC0016703

(D.R., D.C., A.A., J.H.). L.B. acknowledges the US Army Research Office MURI grant W911NF-11-1-0362. The National High Magnetic Field Laboratory is supported by National Science Foundation through NSF/DMR-1157490, NSF/DMR-1644779 and the State of Florida. First-principles calculations by C.D.P. were supported by the TIMES program at SLAC. Numerical simulations were performed using computational resources at the National Energy Research Scientific Computing Center (NSERC). The UED work was performed at SLAC MeV-UED, which is supported in part by the DOE BES SUF Division Accelerator & Detector R&D program, the LCLS Facility, and SLAC under contract Nos. DE-AC02-05-CH11231 and DE-AC02-76SF00515.

Author contributions:
E.J.S., C.M.N., A.M.L. conceived the experiments, analyzed and interpreted the data; E.J.S., C.M.N. performed the SHG experiments, analyzed and interpreted the data with A.M.L., T.F.H.; E.J.S., C.M.N., A.M.L., C.D.P. wrote the manuscript with crucial input from all authors; E.J.S., C.M.N. performed the UED experiments with S.J.P., X.S., J.Y., R.L., S.W., E.M., X.J.W.; B.K.O.-O., M.C.H., A.H.R. implemented the THz setup; D.R., L.B., C.M.N., E.J.S., N.F., D.C., A.A., J.H., T.F.H. synthesized the crystals and prepared the samples; C.D.P., T.P.D. performed the first-principles calculations; X.J.W. led the SLAC 3-MeV UED and THz-pump UED-probe development. All authors discussed the results and contributed to the writing of the manuscript.

Competing interests:
The authors declare no competing interests.

Additional information:
Extended data is available for this paper.

Main figure legends:

Figure 1. Observation of coherent interlayer shear displacements in WTe_2 measured using relativistic ultrafast electron diffraction. (a) Lattice structure of Td-WTe_2 from top view (*a*-*b* plane) and side view (*b*-*c* plane). The dashed lines indicate the W-W zigzag chain along the *a*-axis. The shaded area shows the unit cell. **(b)** Schematic of SLAC 3-MeV relativistic ultrafast electron diffraction setup. The electron beam is generated using ultraviolet femtosecond laser pulses at the photocathode and accelerated using intense radiofrequency field from klystron. The diffracted electron beam is used to probe the structural changes of the sample. Intense THz pump pulses are used to induce interlayer shear strain in WTe_2. **(c)** Measured diffraction pattern of WTe_2 at equilibrium. **(d-e)** Bragg peak intensity changes as a function of time delay between the THz pump pulses and the electron beam. **(f)** FFT amplitude of the oscillations, indicating the 0.24 THz shear phonon mode along the *b*-axis.

Figure 2. Determining the interlayer shear atomic displacements in WTe_2. (a) Measured diffraction intensity changes at 2.5 ps using pump frequency of 23 THz. The alternating sign changes along the *b*-

axis are signatures of shear displacements along the *b*-axis as shown in the inset of panel (e). **(b)** Simulated diffraction intensity changes by rigidly displacing the adjacent WTe_2 layers relative to each other (shear) along the *b*-axis. **(c-d)** Bar charts showing the ΔI fitting results between the experiment and simulation to obtain Δy at pump field of 2.6 MV/cm ($\Delta t = 2.5$ ps) (c) and 7.5 MV/cm ($\Delta t = 70$ ps) (d). **(e)** Energy potential as a function of interlayer shear displacement (DFT calculation, Methods). The schematic shows an interlayer shear motion along the positive displacement, i.e. towards $d_1 < d_3$. Td phase is the ground state noncentrosymmetric structure, whereas 1T′(*) phase is an excited state centrosymmetric structure that is accessible via an interlayer shear displacement. **(f)** Shear displacements as a function of time delay at pump fields 2.6 MV/cm (red) and 7.5 MV/cm (blue), obtained through global fitting of many Bragg peak intensity changes.

Figure 3. Field and polarization dependences of THz-induced shear amplitudes. (a) Bragg peak (130) intensity changes at increasing THz field strength at frequencies of 1.5 and 23 THz. Both experiments show a linear dependence with THz electric field. The vertical error bars represent standard deviations. **(b)** Time-trace at various THz polarizations (23 THz pump), showing that the modulation always starts at the same phase and amplitude regardless of the pump polarization. A similar feature is also observed using 1.5 THz pump. **(c)** Polar plot of the oscillation amplitude at various pump polarization using 1.5 THz (grey circles) and 23 THz (purple circles). The shaded area shows the CCD image of the electron beam transverse displacements by the THz field (streaking), as a measure of the THz pump polarizations. These results show that the driving mechanism of the shear mode is linear in the applied field strength and isotropic in the polarization.

Figure 4. Strain-induced Weyl points separation and topological phase transition. (a) Panels showing the nearest two Weyl points in the momentum space (blue and red) at various shear displacements Δy. **(b)** Topological phase diagram showing the WP separation as a function of shear displacements. **(c)** Time-trace of WP separation upon launching the shear motion using 23 THz pump pulses at fields of 2.5 MV/cm (red) and 7.5 MV/cm (blue). At low fluence, the time-trace shows a clear oscillation toward opening and closing the WP separation. At high fluence, the WPs mostly annihilate each other. **(d)** SHG polar plot of equilibrium WTe_2 (blue), pumped WTe_2 (red), and centrosymmetric $MoTe_2$ (yellow) at various SHG polarizer angle, where the transmission axis is aligned horizontally at 0° angle or vertically at 90° angle. **(e)** Pump-induced SHG time traces of WTe_2 at various pump field strengths. Here, the pump pulse is at 2.1 μm (polarized at 45° off the horizontal axis), the incident probe pulse is at 800 nm vertically polarized, and the crystallographic *a*-axis is aligned horizontally. The SHG results show that WTe_2 exhibits a transition towards a centrosymmetric, topologically trivial phase.

Methods:

Sample synthesis and preparation

High-quality single crystals of WTe_2 were synthesized through a self-flux method in excess of Te: W 99.999% and Te 99.9999% powders were placed in a quartz ampoule in a ratio of 1:25, heated to 1100 °C and held at this temperature for three days. Subsequently, the ampoule was slowly cooled down to 525 °C over two weeks and centrifuged. The "as harvested" single crystals were then annealed for two days at a temperature of 425 °C under a temperature gradient to remove excess Te. To prepare the synthesized samples for UED experiments, WTe_2 was mechanically exfoliated onto a SiO_2/Si substrate using standard mechanical exfoliation technique. From the exfoliated crystal, the samples were selected for subsequent transfer by their size (>50 μm in the lateral dimension) and thickness (>50 nm). After verifying the thickness using an atomic force microscope, poly(propylene carbonate) (PPC) in anisole solution (15% PPC by weight) was spun onto the WTe_2 covered SiO_2/Si substrate at a rate of 1500 rpm with an acceleration of 1000 rpm/s for 1 minute, then heated up to 80 °C for 2 minutes on a hotplate. The PPC film and the WTe_2 crystal were then peeled from the substrate and suspended over a hotplate with the WTe_2 facing up. A 50 nm Si_3N_4 TEM membrane was then aligned over the suspended crystal using an optical microscope and placed on the PPC film while raising the temperature up to 115 °C to induce contact between the WTe_2 crystal and membrane. The sample was then soaked in acetone for 10 minutes to remove the PPC, gently rinsed with isopropyl alcohol, and dried under a flow of nitrogen gas thus completing the transfer.

SLAC 3-MeV Ultrafast Electron Diffraction (UED) setup

We used a relativistic ultrafast electron diffraction (UED) technique to reconstruct the shear motion and crystallographically measure the corresponding atomic displacements through the measurement of more than 200 Bragg peaks (Fig. 1b). The electron beam is generated using a frequency-tripled Ti:sapphire laser by excitation of a copper photocathode, and rapidly accelerated to 3 MeV in radiofrequency electric fields [21]. The pulse duration of the electron beam at the sample position is 150 fs. Magnetic lenses are used to steer and focus the electron beam [31] onto the sample, an exfoliated single-domain crystal, with a spot size of 100 μm. The diffracted electron beam is captured in a transmission geometry using an EMCCD camera. We used two different pump excitation schemes in this experiment, involving a quasi-single cycle excitation at 1-5 THz and a few-cycle excitation at 23 THz. The arrival time of the electron beam (probe) can be adjusted with respect to the THz pulses (pump) using an optical delay stage.

Ultrafast THz sources

Quasi single-cycle THz pulses were generated by optical rectification of 1350 nm near-IR laser pulses in the organic nonlinear crystals DSTMS (4-N,N-dimethylamino-4'-N'-methyl-stilbazolium 2,4,6-trimethylbenzenesulfonate) [32] and OH-1 (2-(3-(4-Hydroxystyryl)-5,5-dimethylcyclohex-2-enylidene)malononitrile) [33]. The 1350 nm near IR pulses were generated from an 800 nm Ti:Sapphire laser system in a three-stage optical parametric amplifier system

(Light Conversion HE-TOPAS) and had pulse energies up to 2 mJ and a pulse duration of ~50 femtoseconds.

The THz field was brought to an intermediate focus with a 2-inch (50.4 mm) focal length off-axis parabolic mirror, collimated with a second, 6-inch (152.4) focal length mirror. The collimated beam was transported into the UED diffraction chamber via a polymer window and focused with a 3-inch (76.2 mm) focal length off-axis parabolic mirror inside the chamber. The THz field was characterized at the sample location by electro-optical sampling using a split-off portion of the 800 nm laser and a 50 μm thick 110-cut GaP crystal. The observed peak field strength of the DSTMS-generated THz pulse was 650 kV/cm, with the spectrum centered at ~3 THz, when using an 8 mm diameter 450 μm thick crystal and ~1 mJ pump pulse energy. With a 10 mm clear aperture, 500 μm thick crystal OH-1 crystal, the peak field strength was 500 kV/cm, with the spectrum peaked at 1.5 THz with significant spectral components extending to about 3.5 THz (Extended Data Fig. 2). The polarization of the THz pulses is linear and the polarization angle can be changed arbitrarily by rotating the generation crystal together with the pump pulse polarization. A detailed discussion of the experimental apparatus can be found in reference [34].

Mid-infrared (MIR) pulses with 13 um wavelength (23 THz frequency) were generated by difference frequency generation in GaSe from the signal and idler of the same Light Conversion HE-TOPAS OPA system driven by ~130 fs duration 800 nm pulses. Here the signal and idler wavelengths were 1505 and 1705 nm, respectively. The MIR beam was transported into the experimental chamber through a 3-mm thick KRS-5 window and focused with a 3-inch (76.2 mm) focal length off-axis parabolic mirror. A pair of holographic wire-grid polarizers (Thorlabs WP25H-K) was used to attenuate the pulse energy to the desired level. The pulse duration of the MIR pulses is on the order of 300 fs after taking into account dispersion. MIR spot-size measurements at the sample position were obtained with a DataRay WinCamD beam profiler.

Structure factor calculation with interlayer shear displacement

The intensity of a Bragg peak, $I \propto |S|^2$, can be calculated using the general form of the structure factor

$$S(hkl) = \sum_j f_j \exp\left(-i2\pi\left(hx_j + ky_j + lz_j\right)\right) \quad (1)$$

where the summation runs over all atoms in the unit cell (4 W and 8 Te), f_j is the atomic scattering factor for j-th atom, $\boldsymbol{r_j} = x_j\hat{a} + y_j\hat{b} + z_j\hat{c}$ is the vector position of the atom in the unit cell ($0 \le x, y, z \le 1$), and (hkl) are the usual Miller indices. Since we use transmission geometry at [001] zone axis, the diffraction image shows only the $l = 0$ peaks, i.e. $(hk0)$. We calculate the peak intensity modulation $\Delta I/I_0$ by introducing the top layer shear displacement Δy with respect to the bottom layer into the structure factor

$$S(\Delta y) = \exp(-i2\pi k\Delta y)\sum_{\text{top}} f_j \exp\left(-i2\pi\left(hx_j + ky_j\right)\right) + \sum_{\text{bottom}} f_j \exp\left(-i2\pi\left(hx_j + ky_j\right)\right) \quad (2)$$

We can obtain a more symmetric expression by having the shear displacement shared equally between the two layers ($\Delta y/2$), i.e. by multiplying with a common phase factor $\exp(+i\pi k\Delta y)$ and by using the underlying crystal symmetry through 1) a reflection with respect to the *b-c* mirror plane ($x \to -x$) and 2) a non-symmorphic C_2 transformation. The latter consists of a reflection with respect to the *a-c* mirror plane ($y \to -y$) and a translation along the *a-c* axis (+0.5, 0, +0.5). These symmetry operations project each atom from the bottom layer to the top layer:

$$\begin{aligned} S(\Delta y) &= \exp(-i\pi k\Delta y)\sum_{\text{top}} f_j \exp\left(-i2\pi\left(hx_j + ky_j\right)\right) \\ &\quad + \exp(+i\pi k\Delta y)\sum_{\text{top}} f_j \exp\left(+i2\pi\left(hx_j + ky_j\right)\right) \\ &= 2\sum_{\text{top}} f_j \cos\left(2\pi\left(hx_j + ky_j\right) + \pi k\Delta y\right) \end{aligned} \quad (3)$$

Now the summation runs over all atoms in the top half of the unit cell (2 W and 4 Te). To compare this with our experiment, we calculated the change of peak intensity $\Delta|S(\Delta y)|^2 = |S(\Delta y)|^2 - |S(0)|^2$ using known x_j and y_j values [16], and plot the image in Figure 2b. The structure factors f_j were calculated using x-ray scattering factors from published analytical fits [35, 36] converted to electron scattering factors using the Mott-Bethe formula [37]. Here, we define a positive shear displacement ($\Delta y > 0$) as shown in the inset of Figure 2e.

Fitting the structural factor modulations

For each time point Δt, the mean squared error (R) is calculated for a range of shear displacements Δy for a selection of m Bragg peaks (hkl). In addition, an anisotropic (elliptical) Debye-Waller factor is included to account for heating effects in the sample, which is significantly smaller than those from the shear displacements due to the low pump photon energy (THz). The mean squared error is:

$$R(\Delta y, \langle u_a^2\rangle, \langle u_b^2\rangle) = \frac{1}{m}\sum_{hkl}\left(\frac{\Delta I}{I_0}(hkl, \Delta y, \langle u_a^2\rangle, \langle u_b^2\rangle)_{\text{sim}} - \frac{\Delta I}{I_0}(hkl)_{\text{exp}}\right)^2$$

where $\langle u_a^2\rangle$ and $\langle u_b^2\rangle$ are the mean squared atomic displacements along the *a* and *b* axes, respectively, which affect the intensity of a Bragg peak by the Debye-Waller relation, $I = I_0 e^{-\frac{1}{2}(Q_a^2\langle u_a^2\rangle + Q_b^2\langle u_b^2\rangle)}$ with a time constant determined by the (400) Bragg peak. Here, Q_a and Q_b are the projections of $\boldsymbol{Q}$, the reciprocal lattice vector of the Bragg peak, along the *a* and *b* axes. The simulated intensity change, $(\Delta I/I_0)_{\text{sim}}$, has the form:

$$\frac{\Delta I}{I_0}(hkl, \Delta y, \langle u_a^2 \rangle, \langle u_b^2 \rangle)_{\text{sim}} = \frac{|S(\Delta y)|^2 e^{-\frac{1}{2}(Q_a^2 \langle u_a^2 \rangle + Q_b^2 \langle u_b^2 \rangle)} - |S(0)|^2}{|S(0)|^2}$$

Here, $S(\Delta y)$ is the structure factor calculated for a given Δy as shown in the main text and $S(0)$ is the structure factor calculated for the undistorted structure. The values for each parameter $\Delta y, \langle u_a^2 \rangle$, and $\langle u_b^2 \rangle$ at every Δt are optimized by minimizing R. In other words, the fitting procedure is performed to minimize the peak intensity difference between experiment and simulation and is averaged across the many Bragg peaks.

Estimating the effective THz-induced hole doping

We use a simple Drude model to estimate the effective hole doping. The fraction of electrons that contribute to the resulting current is v/v_F, where v is the drift velocity and v_F is the Fermi velocity. The drift velocity can be estimated through $v = eE\tau/m$, where e is the electron charge, E is the applied electric field, τ is the scattering time, and m is the effective mass. By using the reported values of m ~0.4 m_e, v_F ~3×10^5 m/s [17], a typical value of $\tau \sim$ 10 fs in a semimetal, and taking E ~1 MV/cm, we found that $v \sim v_F$. For a hole pocket with carrier density of n_0 ~7×10^{19} cm^{-3} in WTe_2 [38], this is comparable with an effective hole doping density required for the Td-1T′ phase transition [22] as the impulsive driving force for the interlayer shear motion. Moreover, recent experiments reported significantly larger scattering time values of $\tau >$100 fs in WTe_2 [17, 39]. This suggests that an even larger electron density can be transiently transferred away from the topmost valence band by the THz pump field to induce the interlayer shear motion. We note that the THz-induced effective doping serves as an impulsive driving force to kick-start the shear mode, and does not require the excited carriers to be maintained during the long-lived metastable phase. Such metastable phase persists for a duration that is determined by the energy barrier of the local potential minimum and thermal fluctuations.

DFT analysis

Density Functional Theory (DFT) [40, 41] simulations of WTe_2 were carried out to ascertain the energetics of the experimentally observed 0.24 THz shear mode of interest (Fig. 2e of the main text) and the Brillouin-zone (BZ) motion of Weyl points resulting from atomic displacements associated with this mode. The topological characteristics of the electronic band structure of Td-WTe_2 have been explored previously in the literature [16, 22]. In particular, Soluyanov et al [16] investigated the Type-II Weyl semimetal character of Td-WTe_2 based partly on DFT bandstructure simulations carried out at the experimentally observed geometry [42]. More recently, Kim et al [22] studied the effect of geometry optimization, within the van der Waals (vdW) DFT framework [43], on the Weyl points in Td-WTe_2. They found that the stability of Weyl nodes in WTe_2 is sensitive to lattice parameter differences on the order of 1% and, in fact, due to slight (~1%) inaccuracies in the vdW-DFT predicted *a* and *c* parameters, Weyl points of opposite chiralities annihilate at the vdW-DFT equilibrium geometry of WTe_2 rendering it a trivial semimetal. To recover distinct Weyl nodes in the BZ, small strains need to be applied [22].

In order to circumvent the issues related to the sensitive dependence on specific vdW-DFT geometries, we initially employ as reference the experimental geometry [42] used in the work of Soluyanov et al [16] to carry out our analysis of the BZ motion of the Weyl nodes in WTe_2 under the influence of shear-mode displacements along the y-axis (crystallographic *b*-axis). This geometry is characterized by an orthorhombic (Td) lattice, with parameters a = 3.477 Å, b = 6.249 Å and c = 14.018 Å. W and Te atoms occur at the 2a Wyckoff positions parameterized as (0, y, z) and (1/2, -y, z+1/2) for values of y, z given in Table S1 (reproduced from Soluyanov et al [16]). Simulations in this context are carried out using the DFT framework as implemented in the Vienna *Ab initio* Simulation Package [44] (VASP) version 5.4.1. All calculations include spin-orbit coupling (SOC) within the non-collinear DFT formalism. Exchange-correlation (XC) effects are treated at the level of the generalized gradient approximation through the PBE [45] functional. Projector augmented wave [46] (PAW) potentials with valence electronic configurations of $\{6s^2,5d^4\}$ for W and $\{5s^2,5p^4\}$ for Te are employed in conjunction with a plane-wave energy cutoff parameter of 260 eV. For converging the electron density, a Γ-centered 12x10x6 k-point grid and Gaussian smearing with a smearing parameter of 0.05 eV are used. The simulation parameters here are similar to the ones adopted in the work of Soluyanov et al [16]. Weyl point positions in the $k_z = 0$ plane of the BZ of WTe_2 are subsequently identified through band structure calculations employing a dense 43x85x1 k-point mesh spanning a sub-region of the $(k_x, k_y, k_z = 0)$ plane as shown in Fig. 4a of the main text. At the employed geometry, we identify two Weyl points (WP1, WP2) in the first quadrant of the $k_z = 0$ plane of the BZ at the coordinates shown in Table S2. The remaining 6 points in the other three quadrants are related to these by reflections in the $k_x = 0$ and $k_y = 0$ planes [16]. The coordinates identified here are similar to those reported in the literature [16, 22].

Table S1. Wyckoff position parameters for the coordinates of W and Te atoms in the experimentally determined [16, 42] unit cell of WTe_2

	W(1)	W(2)	Te(1)	Te(2)	Te(3)	Te(4)
y	0.60062	0.03980	0.85761	0.64631	0.29845	0.20722
z	0.5	0.01522	0.65525	0.11112	0.85983	0.40387

Table S2. Coordinates and Chern numbers of the two Weyl points occurring in the first quadrant of the $k_z = 0$ plane of the BZ of WTe_2. The last column indicates the Chern number (C) of the nodes.

	k_x	k_y	k_z	C
WP1	0.12195	0.03947	0	+1
WP2	0.12160	0.04510	0	-1

Phonon band-structures are calculated within the frozen-phonon finite-difference approach using the phonopy [47] code interfaced with VASP. In Extended Data Fig. 3, the phonon band dispersions of Td-WTe_2 at the experimental reference geometry, are plotted along high-

symmetry lines in the $k_z = 0$ plane. At the Γ-point, the low-energy mode at 0.29 THz is unambiguously identified as the relevant interlayer shear mode of interest, which corresponds to the 0.24 THz mode observed experimentally. This identification is facilitated by the absence of any other modes at similar energies and also by inspecting the atomic position modulations associated with the mode-eigenvector. As denoted in Figure 2e of the main text, this mode predominantly involves a relative shear displacement along the *b*-axis, of adjacent WTe_2 layers in the unit cell. To investigate the motion of Weyl points in the BZ induced by this mode, firstly a number of unit cell geometries modulated along the mode displacement coordinate are generated using the phonopy code. Subsequently, the DFT electronic band structures corresponding to these modulated geometries are calculated and the positions of Weyl points in the BZ as are mapped as a function of displacement along the mode coordinate as shown in Figure 4a of the main text. As explained in the main text in connection with Figure 4a, depending upon the sign of the shear mode displacement along the *b*-axis, pairs of Weyls points either move closer or farther apart in the BZ leading to different kinds of topological transitions.

In topological semimetals such as WTe_2, the positions of Weyl points in the BZ can be tuned by applying strain. Soluyanov et al [16] explored changes in the relative positions of Weyl nodes in WTe_2 induced by uniaxial tensile and compressive strains applied along different crystallographic axes. They report that while stretching along the *a*-axis leads to annihilation of all pairs of Weyl nodes, compressive strain along this direction leads to increased separation within each pair of Weyl points until half the points eventually annihilate on the $k_y = 0$ mirror plane leading to a state where only four Weyl nodes survive. In this work, as explained in the analysis accompanying Figure 4 of the main text, we find that a similar motion of the Weyl points can be induced via an alternate mechanism, namely THz-pump induced phonon modulations associated with the 0.24 THz shear-mode along the *b*-axis. It is therefore instructive to evaluate the relative energy cost associated with these two approaches for tuning the topological properties of WTe_2. To this end we compare DFT total energies of different strained and phonon modulated structures associated with the Weyl point motion described in Figure 4 of the main text. Calculating the total energy cost under different deformations of the lattice requires identifying the minimum energy point associated with the equilibrium geometry. Therefore, for this analysis, we first carry out geometry optimizations within the dispersion corrected DFT-D3 [48] framework including spin-orbit coupling as implemented in VASP. A plane-wave cutoff of 400 eV in conjunction with a Γ-centered 16x9x4 k-point grid is employed in this instance. As before, XC effects are modeled using the PBE functional and additionally, dispersion corrections are incorporated at the level of the DFT-D3 [48] approximation. In particular, for reasons explained below, two different forms for the dispersion corrections are investigated, namely DFT-D3 [11] (labelled D3) and DFT-D3 with Becke-Johnson (BJ) damping [49] (labelled D3-BJ). The lattice parameters and relevant interlayer distances d_1, d_2, d_3 (see Figure 2e of main text) in Td-WTe_2 predicted by the two methods are listed in Table S3 and compared to experimental values.

Table S3. Calculated lattice and interlayer distance parameters of Td-WTe_2 are compared to experiment. The last column shows the calculated phonon frequency of the *b*-axis shear mode of interest.

	a (Å)	*b* (Å)	*c* (Å)	d_1 (Å)	d_2 (Å)	d_3 (Å)	ν_{shear} *(THz)*
D3	3.4807	6.2806	13.9973	5.3104	3.8734	5.0137	0.15
D3-BJ	3.4841	6.2528	13.5910	5.2570	3.7169	4.7787	0.34
Experiment [5]	3.477	6.249	14.018	5.397	3.911	4.937	0.24

The last column of Table S3 shows the calculated and experimental phonon frequency for the *b*-axis shear mode. As mentioned earlier, this mode is well-approximated as a rigid relative motion along the *b*-axis, of the two WTe_2 layers in the unit cell (see Extended Data Fig. 3). The potential energy associated with this motion is predominantly determined by the interlayer vdW interaction, at least for small displacements, and therefore exhibits a strong dependence on the way the dispersion corrections are approximated in DFT. We note that while the D3 method yields lattice parameters that are within 0.5% of experiment, the *b*-axis shear mode phonon frequency is underestimated by ~37%. On the other hand, the D3-BJ approximation predicts a mode frequency that is overestimated by ~40%. In the harmonic approximation within which the phonon frequency is estimated, this corresponds to a picture where the potential energy surface associated with displacement along the shear mode is too shallow and too steep in the D3 and D3-BJ approximations respectively. Although neither method is quantitative, we expect that the correct description lies in between the two limits represented by D3 and D3-BJ. With this understanding, we provide here an order of magnitude comparison between the relevant strain and phonon modulation energies for driving Weyl point motion in WTe_2. Referred to the equilibrium geometry, the total energy cost per unit cell as a function of applied compressive strain along the *a*-axis is shown in Extended Data Fig. 4a. Similarly, the total energy cost associated with structural modulation by the *b*-axis shear phonon as function of displacement along the mode coordinate is shown in Extended Data Fig. 4b. The displacement (in pm) along the *b*-axis, of one of the W atoms is used as a proxy for the mode coordinate. In order to annihilate two pairs of Weyl nodes at the $k_y = 0$ mirror plane, either a 2% *a*-axis compressive strain [16] or a ~12 pm negative displacement in the sense of Figure 2e of the main text is required. On a per unit cell basis, in the D3 (D3-BJ) approximation the former mechanism has an energy cost of 32 meV (39 meV) while the latter costs 0.33 meV (3.6 meV). Thus for driving the topological transition from eight to four Weyl nodes, the lattice strain mechanism is one to two orders of magnitude more expensive compared to the phonon driven mechanism in terms of energy. This is expected since an *a*-axis strain involves compressing or elongating strong covalent bonds within each layer of WTe_2 while *b*-axis shear mode involves primarily interlayer interactions which are weaker.

Longitudinal acoustic wave timescale

In WTe_2, the stable Td phase appears as an orthorhombic unit cell where the b-c axes make a $\theta = 90°$ angle, while the 1T′ phase appears as a monoclinic unit cell with 94° angle (Extended Data Fig. 1). Hence, we can expect the Td-1T′ transition in WTe_2 to be limited by the timescale for the development of an overall shear across the sample thickness (c-axis), as determined by the transverse acoustic group velocity. While we are not aware of any prior measurements on the transverse acoustic (TA) velocity, we can take the longitudinal acoustic (LA) speed of sound as a first approximation of 2000 m/s [50]. Hence, we can estimate the buildup time through $t = d/v$, where d (= 50 nm) is the sample thickness and v (= 2000 m/s) is speed of sound, and obtain $t =$ 25 ps. This is in good agreement with our observation (Fig. 2f, blue). We can take a separate confirmation of the LA speed of sound by tilting the sample (Pitch $= -8.3°$, Yaw $= -13.9°$), providing sensitivity to the acoustic breathing mode oscillations (period $= 2d/v$) across the sample thickness. The structural factor modulation $\Delta I/I_0$ of peak $(13\bar{3})$ shows oscillations with period of 38 ps (Extended Data Fig. 5). Given the period of this oscillation, we compute the speed of sound to be $v \sim 2600$ m/s, in reasonable agreement with the above estimate.

THz-induced shear motion in $MoTe_2$

We discussed in the main text that the shear motion in WTe_2 is driven through a transient hole doping induced by the THz field. This interpretation is motivated by a theoretical prediction that upon hole doping the Td phase becomes unstable against the 1T′ phase [22]. A particularly strong indication we found from our experiment is that at any THz field polarization the initial shear motion always occurs along the pathway towards a phase transition from Td phase to 1T′ phase. Hence, this process must be very sensitive to the initial structural phase of the sample, i.e. it should only occur in Td phase and not in 1T′ phase, a feature that can be tested. In particular we should expect the absence of THz-induced shear motion in 1T′-$MoTe_2$. $MoTe_2$ and WTe_2 have similar structural and electronic properties; unlike WTe_2, however, $MoTe_2$ can appear in two structural phases: Td phase below 200 K, 1T′ phase above 250 K, and mixed Td-1T′ phase between 200-250 K [25]. We performed similar THz-pump UED-probe experiments on $MoTe_2$ at sample temperatures of 28 K (Td) and 300 K (1T′) (Extended Data Fig. 6). We found that the interlayer shear oscillations only occur in the Td phase (0.37 THz), and not in the 1T′ phase of $MoTe_2$ where only a small heating (Debye-Waller) effect is observed. This is consistent with the picture that THz-induced hole doping stabilizes the 1T′ phase over the Td phase. That is, if we start with Td phase the relative energy order is reversed upon THz-induced hole doping and shear motion is launched, but if we start with 1T′ phase the relative energy order does not change and no shear motion is observed.

Transition region at intermediate pump fluences

The UED time-traces (Fig. 2f, main text) show that the oscillation period is slightly longer at larger pump field strengths. To investigate this transition region, we carried out an additional THz-pump, UED probe at finer changes of pump fluences (Extended Data Fig. 7a-b). As we can

see, the oscillation period increases at higher pump fluences. This observation indicates a nonlinear phonon softening toward a new metastable centrosymmetric structure.

Lifetime of excited electrons

The lifetime of excited electrons can be learned from the pump-induced probe reflectivity as a function of time. We carried out an optical pump-probe experiment using 2.1 μm pump and 800 nm probe pulses on WTe_2 sample (Extended Data Fig. 8). Note that we replace the role of THz pump with a 2.1 μm pump because the THz pump setup we used for UED requires a special laser specification and is currently not accessible for optical reflectivity experiment. Nevertheless, measurements with 2.1 μm pump can also induce the shear oscillations that were obtained using THz pump (Extended Data Fig. 9). Extended Data Figure 8 shows an abrupt pump-induced change of probe reflectivity within the first 5 ps, and a stable finite reflectivity afterwards for a timescale longer than 50 ps. The first 5 ps can be attributed to relaxation of hot carriers toward a new quasi-equilibrium state. Afterwards, the carriers remain in the new equilibrium state for longer than 50 ps.

References for Methods:

31. X. Shen et al. "Femtosecond mega-electron-volt electron microdiffraction". *Ultramicroscopy* **184,** 172-176 (2018).
32. Z. Yang et al. "Large-Size Bulk and Thin-Film Stilbazolium-Salt Single Crystals for Nonlinear Optics and THz Generation". *Advanced Functional Materials* **17,** 2018-2023 (2007).
33. F.D. Brunner et al. "A hydrogen-bonded organic nonlinear optical crystal for high-efficiency terahertz generation and detection". *Optics Express* **16,** 16496 (2008).
34. B.K. Ofori-Okai et al. "A terahertz pump mega-electron-volt ultrafast electron diffraction probe apparatus at the SLAC Accelerator Structure Test Area facility". *Journal of Instrumentation* **13,** P06014-P06014 (2018).
35. D. Waasmaier and A. Kirfel. "New analytical scattering-factor functions for free atoms and ions". *Acta Crystallographica Section A Foundations of Crystallography* **51,** 416-431 (1995).
36. Z. Su and P. Coppens. "Relativistic X-ray Elastic Scattering Factors for Neutral AtomsZ= 1–54 from Multiconfiguration Dirac–Fock Wavefunctions in the 0–12Å−1sinθ /λ Range, and Six-Gaussian Analytical Expressions in the 0–6Å−1Range". *Acta Crystallographica Section A Foundations of Crystallography* **53,** 749-762 (1997).
37. M. De Graef, *Introduction to Conventional Transmission Electron Microscopy*. 2003: Cambridge University Press.
38. Z. Zhu et al. "Quantum Oscillations, Thermoelectric Coefficients, and the Fermi Surface of Semimetallic WTe2". *Phys Rev Lett* **114,** 176601 (2015).
39. C.C. Homes, M.N. Ali, and R.J. Cava. "Optical properties of the perfectly compensated semimetalWTe2". *Physical Review B* **92,** 161109 (2015).
40. P. Hohenberg and W. Kohn. "Inhomogeneous Electron Gas". *Physical Review* **136,** B864-B871 (1964).
41. W. Kohn and L.J. Sham. "Self-Consistent Equations Including Exchange and Correlation Effects". *Physical Review* **140,** A1133-A1138 (1965).
42. A. Mar, S. Jobic, and J.A. Ibers. "Metal-metal vs tellurium-tellurium bonding in WTe2 and its ternary variants TaIrTe4 and NbIrTe4". *Journal of the American Chemical Society* **114,** 8963-8971 (1992).
43. I. Hamada. "van der Waals density functional made accurate". *Physical Review B* **89,** 121103 (2014).
44. G. Kresse and J. Furthmüller. "Efficient iterative schemes forab initiototal-energy calculations using a plane-wave basis set". *Physical Review B* **54,** 11169-11186 (1996).

45. J.P. Perdew, K. Burke, and M. Ernzerhof. "Generalized Gradient Approximation Made Simple". *Phys Rev Lett* **77,** 3865-3868 (1996).
46. P.E. Blöchl. "Projector augmented-wave method". *Physical Review B* **50,** 17953-17979 (1994).
47. A. Togo and I. Tanaka. "First principles phonon calculations in materials science". *Scripta Materialia* **108,** 1-5 (2015).
48. S. Grimme et al. "A consistent and accurate ab initio parametrization of density functional dispersion correction (DFT-D) for the 94 elements H-Pu". *J Chem Phys* **132,** 154104 (2010).
49. S. Grimme, S. Ehrlich, and L. Goerigk. "Effect of the damping function in dispersion corrected density functional theory". *J Comput Chem* **32,** 1456-65 (2011).
50. Y. Zhou et al. "Direct Synthesis of Large-Scale WTe2 Thin Films with Low Thermal Conductivity". *Advanced Functional Materials* **27,** 1605928 (2017).

Data availability:

The data that support the findings of this study are available from the corresponding author on reasonable request.

Extended data figure legends:

Extended Data Figure 1. Lattice structures of **(a)** Td **(b)** 1T′(*) and **(c)** 1T′ phase. Td phase has an orthorhombic non-centrosymmetric unit cell with *b*-*c* angle of 90° and bond length $d_1 > d_3$. 1T′(*) phase has an orthorhombic centrosymmetric unit cell with *b*-*c* angle of 90° and bond length $d_1 = d_3$. 1T′ phase has a monoclinic centrosymmetric unit cell with *b*-*c* angle of ~94° and bond length $d_1 < d_3$.

Extended Data Figure 2. Electro-optical sampling data for the quasi single-cycle THz pulses generated in OH1 and DSTMS and their amplitude spectra. **(a)** THz electric field time trace. **(b)** Frequency bandwidth of the THz field, calculated using the Fourier transform of panel (a).

Extended Data Figure 3. Phonon band structure of Td-WTe_2. Dispersions for wave-vectors along high-symmetry lines in the $k_z = 0$ plane are shown. The schematic on the right shows the interlayer shear motion as rigid displacements between WTe_2 alternating layers.

Extended Data Figure 4. (a) Energy as a function of uniaxial strain applied along the *a*-axis. We used two different forms for the dispersion corrections, namely DFT D3 and DFT D3-BJ with Becke-Johnson (BJ) damping. These two corrections result in slightly different lattice constants, as shown in Table S3, and yield potential energy surfaces that are too shallow and too steep in the D3 and D3-BJ approximations respectively. The correct description lies in between the two limits represented by D3 and D3-BJ. **(b)** Energy as a function of displacement along the shear mode coordinate. The red dashed line indicates the displacement at which two pairs of Weyl nodes annihilate at the $k_y = 0$ mirror plane (see Figure 4 of main text).

Extended Data Figure 5. Determining the transverse acoustic propagation time across the sample thickness.

Extended Data Figure 6. The emergence of THz-induced shear oscillations in Td-$MoTe_2$, and not in 1T′-$MoTe_2$.

Extended Data Figure 7. Additional THz-pump UED probe measurements at various pump fluences to demonstrate the evolution in the transition region towards the switching behavior. **(a)** Intensity changes of (130) Bragg peak show the interlayer shear oscillation that exhibits a phonon softening at larger pump fluences. **(b)** Surface plot of panel (a) where the $\Delta I/I_0$ is shown by the color scale. We use interpolation in panel (b) to show a clearer picture on the frequency shifting at larger pump fluences.

Extended Data Figure 8. Pump-induced reflectivity changes on WTe_2. The pump pulse is at 2.1 μm and the probe pulse at 800 nm. Transient reflectivity gives a direct experimental probe to the electronic system. There is an abrupt change of $\Delta R/R$ right after the pump pulse arrival, within 5 ps timescale. Afterwards, the $\Delta R/R$ signal remains finite and stable for a timescale longer than 50 ps.

Extended Data Figure 9. Bragg peak intensity changes as a function of time delay between the 2.1 μm pump pulses and the electron beam. The intensity changes show oscillations that correspond to the interlayer shear mode frequency of 0.24 THz, similar to the effect produced by THz pump pulses shown in the main text.

Extended Data Figure 10. Time-resolved SHG of WTe_2 at nanosecond time delay. Here, the pump pulse is at 2.1 μm (polarized at 45° off the horizontal axis), the incident probe pulse is at 800 nm, the crystal *a*-axis is aligned horizontally, and the SHG is detected at "S-in P-out" configuration. This shows that the light-induced centrosymmetric phase lives for a few nanoseconds or even tens of nanoseconds, which is consistent with the induced metastable phase discussed in the main text.

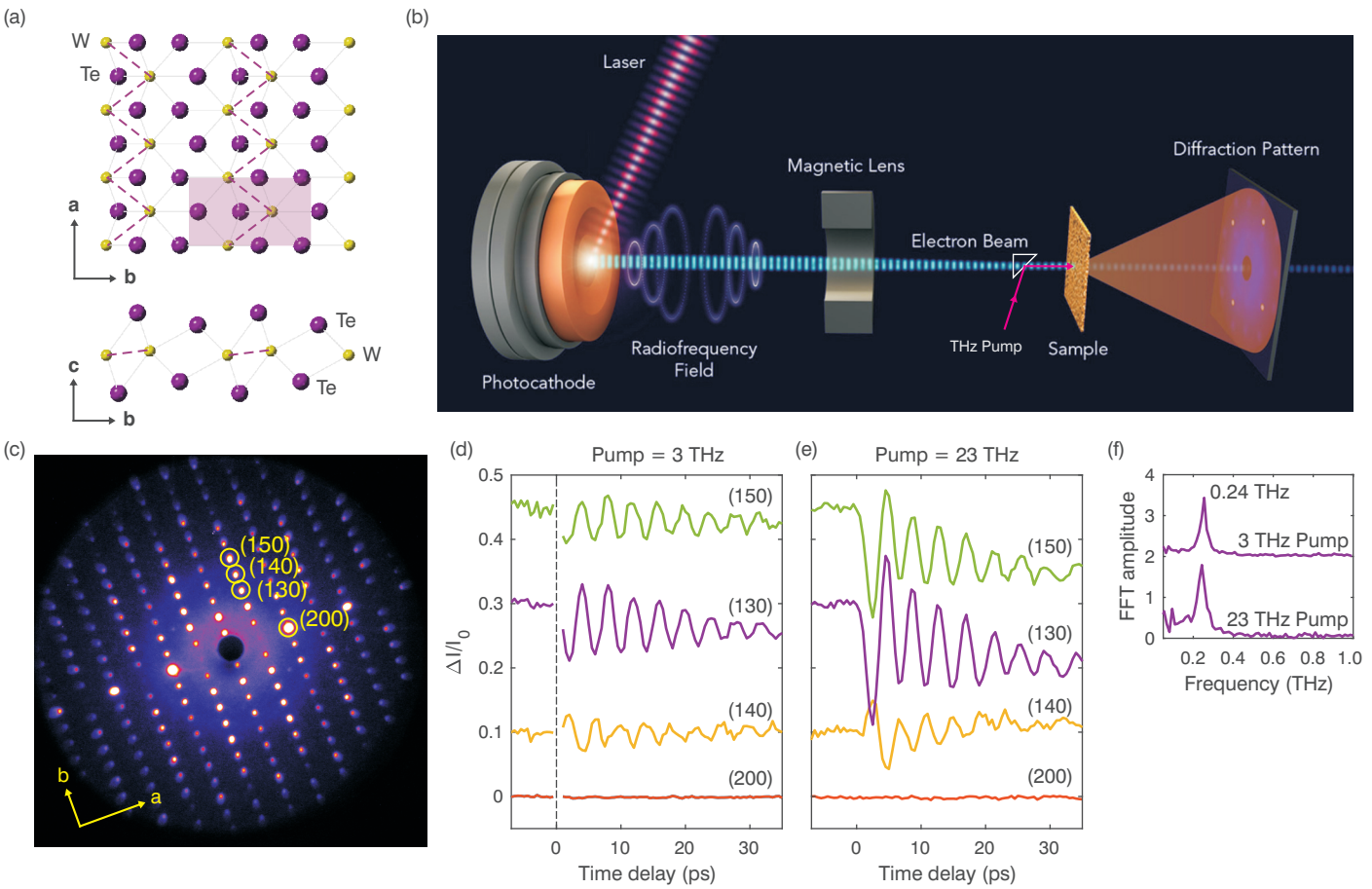
(a)
W
Te
a
b
Te
W
Te
c
b
(b)
Laser
Magnetic Lens
Diffraction Pattern
Electron Beam
Radiofrequency
Field
THz Pump
Sample
Photocathode
(c)
(150)
(140)
(130)
(200)
b
a
(d)
Pump = 3 THz
(150)
(130)
(140)
(200)
ΔI/I0
Time delay (ps)
(e)
Pump = 23 THz
(150)
(130)
(140)
(200)
Time delay (ps)
(f)
0.24 THz
3 THz Pump
23 THz Pump
FFT amplitude
Frequency (THz)

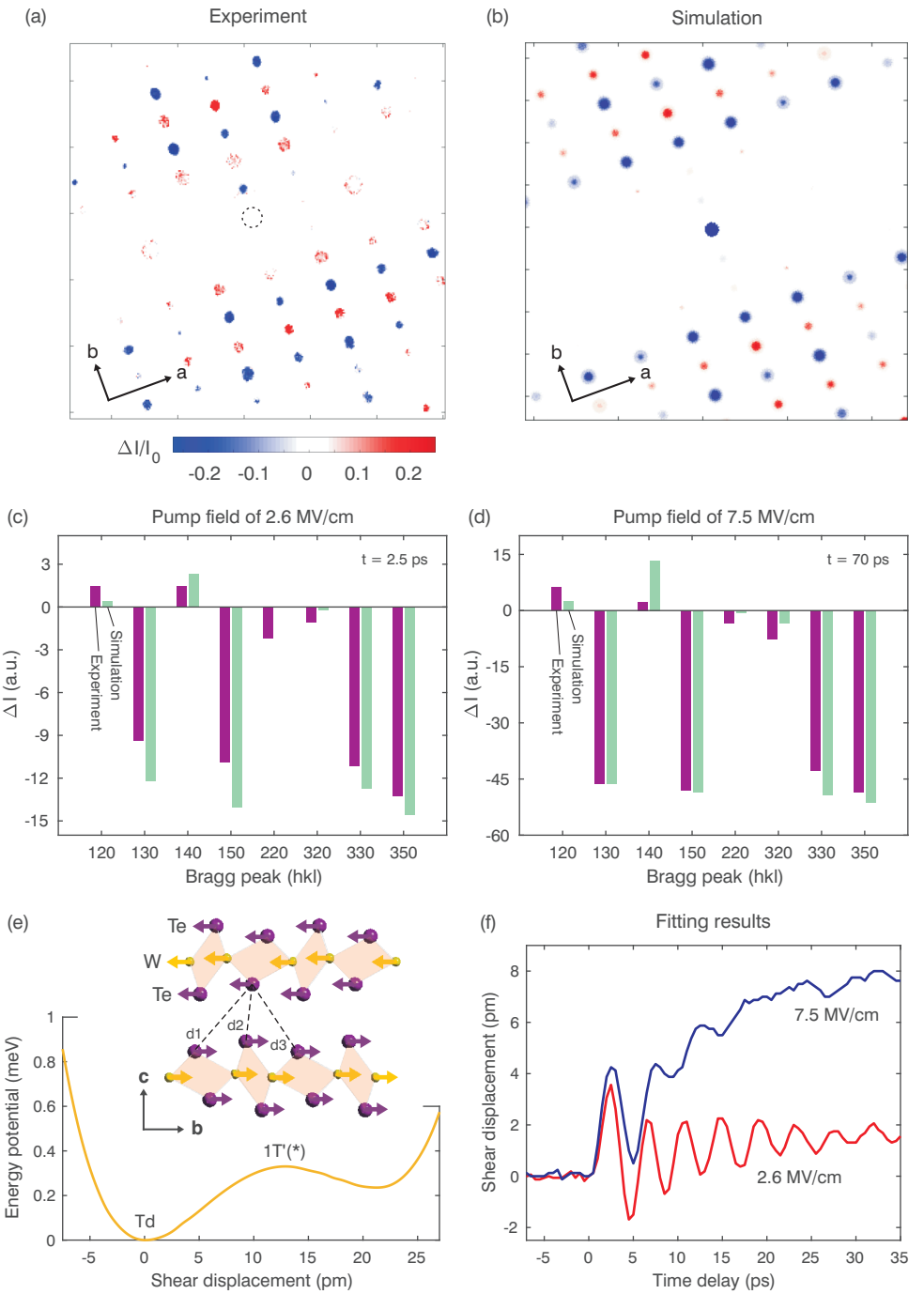
(a)
Experiment
(b)
Simulation
b
a
ΔI/I0
-0.2 -0.1 0 0.1 0.2
(c)
Pump field of 2.6 MV/cm
t = 2.5 ps
Simulation
Experiment
ΔI (a.u.)
Bragg peak (hkl)
(d)
Pump field of 7.5 MV/cm
t = 70 ps
(e)
Te
W
Te
d1
d2
d3
c
b
1T'(*)
Td
Energy potential (meV)
Shear displacement (pm)
(f)
Fitting results
7.5 MV/cm
2.6 MV/cm
Shear displacement (pm)
Time delay (ps)

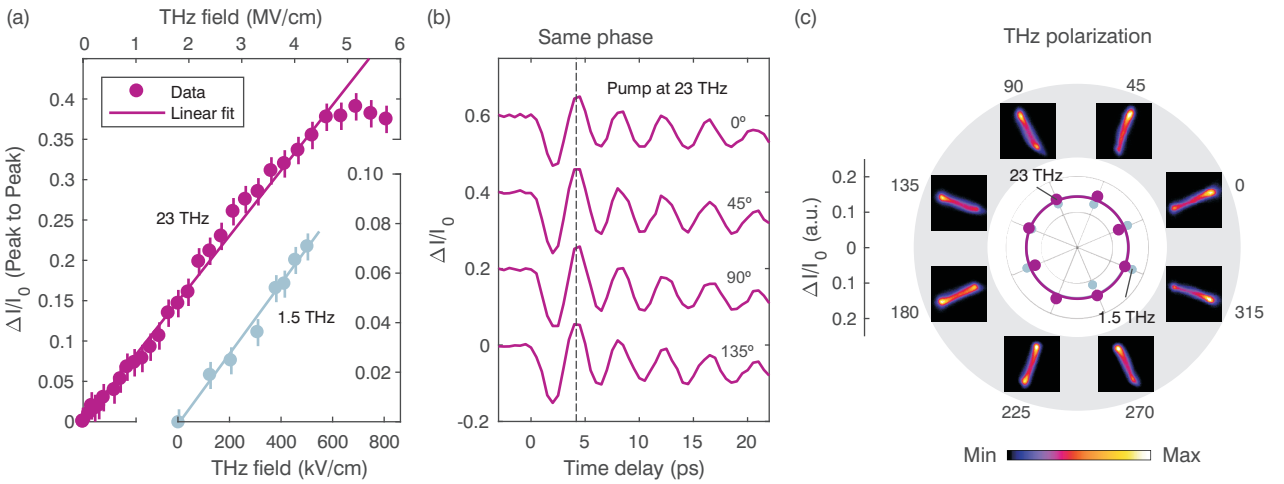
(a)
THz field (MV/cm)
Data
Linear fit
23 THz
1.5 THz
ΔI/I0 (Peak to Peak)
THz field (kV/cm)
(b)
Same phase
Pump at 23 THz
0°
45°
90°
135°
ΔI/I0
Time delay (ps)
(c)
THz polarization
90
45
135
0
180
315
225
270
23 THz
1.5 THz
ΔI/I0 (a.u.)
Min
Max

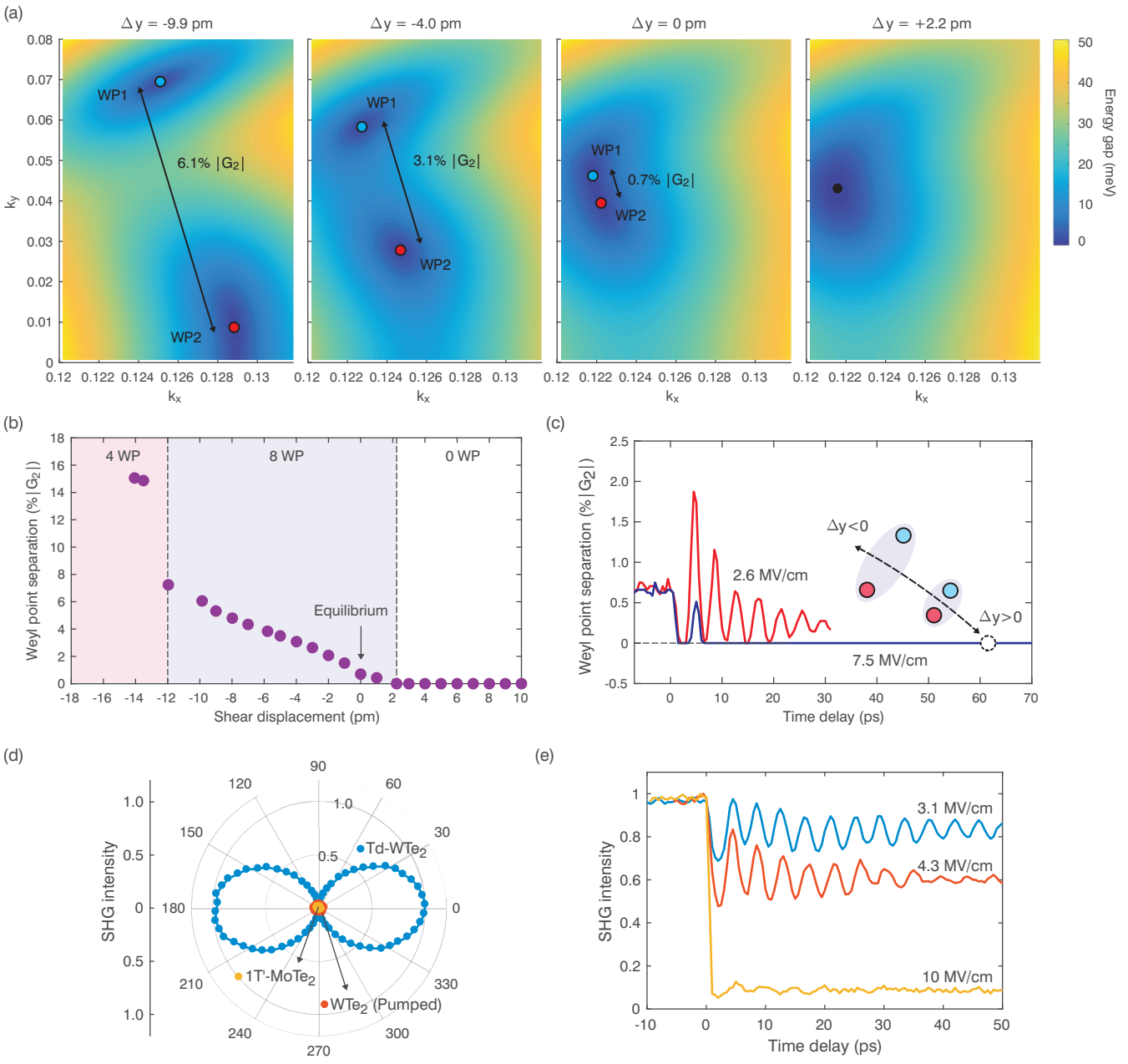
(a)
Δy = -9.9 pm
Δy = -4.0 pm
Δy = 0 pm
Δy = +2.2 pm
WP1
WP2
6.1% |G2|
3.1% |G2|
0.7% |G2|
ky
kx
Energy gap (meV)
(b)
4 WP
8 WP
0 WP
Equilibrium
Weyl point separation (% |G2|)
Shear displacement (pm)
(c)
Δy<0
Δy>0
2.6 MV/cm
7.5 MV/cm
Weyl point separation (% |G2|)
Time delay (ps)
(d)
Td-WTe2
1T'-MoTe2
WTe2 (Pumped)
SHG intensity
(e)
3.1 MV/cm
4.3 MV/cm
10 MV/cm
SHG intensity
Time delay (ps)